Research Article Vol. 28, No. 11 / 25 May 2020 / Optics Express 16594
Optics EXPRESS

Graphene-based ultrasensitive optical microfluidic sensor for the real-time and label-free monitoring of simulated arterial blood flow

TIANGE WU,[1,4] JUNFENG SHEN,[2,4] ZONGWEN LI,[1,4] TINGTING ZOU,[3] WEI XIN,[3] FEI XING,[1,5] FANG ZHANG,[1] ZHONGSHENG MAN,[1] AND SHENGGUI FU[1,6]

[1]School of Physics and Optoelectronic Engineering, Shandong University of Technology, Zibo 255049, China
[2]School of Physical Science and Technology, Southwest Jiaotong University, Sichuan 614202, China
[3]The Guo China-US Photonics Laboratory, State Key Laboratory of Applied Optics, Changchun Institute of Optics, Fine Mechanics, and Physics, Chinese Academy of Sciences, Changchun, China
[4]These authors equally contributed to this work
[5]xingfei@sdut.edu.cn
[6]fushenggui@163.com

Abstract: Highly sensitive, real-time and label-free sensing of liquid flow in microfluidic environments remains challenging. Here, by growing high-quality graphene directly on a glass substrate, we designed a microfluidic-integrated graphene-based flow sensor (GFS) capable of detecting complex, weak, and transient flow velocity and pressure signals in a microfluidic environment. This device was used to study weak and transient liquid flows, especially blood flow, which is closely related to heart and artery functions. By simulating cardiac peristalsis and arterial flow using peristaltic pumps and microfluidic systems, we monitored simulated arterial blood flow. This ultrasensitive graphene-based flow sensor accurately detected a flow velocity limit as low as 0.7 mm/s, a pumping frequency range of 0.04 Hz to 2.5 Hz, and a pressure range from 0.6 kPa to 14 kPa. By measuring the blood flow velocities and pressures, pathological blood flow signals were distinguished and captured by the corresponding flow velocities or pressures, which can reflect vascular occlusion and heart functions. This sensor may be used for the real-time and label-free monitoring of patients' basic vital signs using their blood flow and provide a possible new method for the care of critically ill patients.

1. Introduction

Microfluidic flow velocity and pressure, especially blood flow velocity and pressure which can prevent and diagnose certain diseases, are important parameters in medicine and disease prevention [1–10]. International research teams are working to develop highly-sensitive, real-time, label-free blood flow sensing methods. Early efforts involved fiber-optic flow sensing [11] and heat-washout measurements [12], while more mature methods involve Doppler flow measurements [13–15]. The heat-washout method uses heat as an indicator by exploiting the fact that blood is the main heat transfer medium in the human body, and measures the blood flow velocity by measuring the temperature change in an electrode in contact with human skin. However, this relatively new method has too many problems to be more broadly used due to the immature technology. Both fiber optic flow sensing and Doppler flow measurement technologies have been implemented which are based on Doppler frequency shifts, in which frequency-shifted signals related to blood flow are extracted for processing. However, this technique is expensive to implement and is difficult to use in real-time sensing. In addition, existing flow sensors can

#392993 https://doi.org/10.1364/OE.392993
Journal © 2020 Received 18 Mar 2020; revised 28 Apr 2020; accepted 11 May 2020; published 18 May 2020

Optics EXPRESS

only detect single flow parameter (flow velocity or pressure). Therefore, designing a novel flow sensor, which performs the real-time and label-free detection of complex, weak, and transient flow velocities and pressures in microfluidic environments remains challenging.

Graphene is a novel 2D material that has been used in the sensing field because of its ultrafast electrical and optical properties [16–28]. In reflection-coupling structures, graphene exhibits outstanding sensing characteristics [26–28]. We previously showed that a graphene layer exhibited different absorption behaviors in the transverse-magnetic (TM) and transverse-electric (TE) modes [29]. Additionally, the absorption in both TE and TM modes was sensitive to variations in the refractive index [26]. Based on this property of graphene, we established an ultrasensitive RI sensor with a RI resolution of 10^{-8} RIU, which is the highest value reported [26]. The refractive index is linearly related to the liquid flow velocity and pressure in microfluidic environments. Therefore, by combining the polarization absorption characteristics of graphene with a microfluidic system, we developed an ultrasensitive flow sensor to accurately detect liquid flow velocity and pressure in real-time without labeling. Furthermore, we used a peristaltic pump equipped with the GFS to simulate cardiac peristalsis and monitor blood flow velocity, which is believed to be a promising candidate for monitoring patients with heart or vascular disease.

Chemical vapor deposition (CVD) provides a relatively low-cost method for growing graphene that is compatible with chip fabrication processes [16,30,31]. In this paper, ethanol was used as a precursor to directly grow graphene on an insulating glass substrate using CVD in a low-pressure environment. The preparation of graphene by CVD method has many merits: i) the deposition process is simple; ii) the carbon source for film formation is easy to obtain and its cost is low; iii) graphene can be prepared in a large area; iv) the thickness and characteristics of the film can be easily controlled by changing and adjusting the proportion of reactants, thus the flexibility is greater. Graphene-prepared electronic devices or experimental chips grown on metal substrates using CVD cannot be directly applied to transparent media, and the graphene must first be completely transferred from a metal growth substrate to an insulating substrate. The goal is to obtain neat and high-quality graphene without introducing any additional structural defects or surface contamination during the transfer process. Nevertheless, problems including film damage, contamination, and high surface roughness values are inevitable after the transfer process, which reduces the success rate of device fabrication and uniform performance. In order to solve these problems, we improved our method by growing graphene on glass with a growth pressure below 300 Pa and a gas flow rate below 100 sccm. Graphene's adhesion to glass was significantly enhanced under these low-pressure conditions. In a low-pressure environment, surface reactions are one of the pivotal factors determining the rate of graphene synthesis. The active carbon material is highly diffused in a low-density environment, which gives the system a fairly high mass-transport rate and a comparatively uniform distribution of activated carbon [32,33]. Furthermore, the selection of a suitable carbon precursor for growing graphene under low-pressure conditions can improve graphene's uniformity and growth efficiency [34]. We choose ethanol as the precursor due to its low probability of collision with activated carbon materials in a low-pressure environment, and the etching effect of the hydroxyl groups greatly limits the formation of amorphous carbon materials. In addition, ethanol can be thermally decomposed at temperatures greater than 800 °C to provide sufficient active carbon species for graphene nucleation and growth [35,36], which further improves the growth efficiency of graphene. Typically, a long synthesis cycle is required to grow graphene on glass. However, the low-pressure chemical vapor deposition (LPCVD) method uses ethanol as a precursor to rapidly and evenly deposit graphene on glass, and monolayer graphene coverage on glass substrates can be achieved in just a few minutes [31].

Optics EXPRESS

2. Materials and methods

2.1. Preparation of graphene

Graphene glass grown by the LPCVD method was used in the experiment. First, the glass was polished with a high-precision polishing machine to obtain a smooth optical surface. Then, the glass was immersed in a solution of water, isopropanol, and acetone for ultrasonic cleaning for 15 minutes. Finally, the cleaned glass was dried with N_2. The temperature of a tube furnace was set to 1050 °C, and then the cleaned glass-jacketed quartz tube was placed in the furnace. In the preparation of graphene, ethanol was used as the carbon source, Ar and H_2 were used as carrier gases. Each valve control switch ensured airtightness, and the vacuum pump was opened. The actual pressure of the chamber is maintained at 1000-1500 Pa through the vacuum pump in the reaction state. Then, Ar and H_2 were successively introduced, and the flowmeter connected to the ethanol tank was opened. The flow rate of ethanol was set to 200 sccm, the flow rates of Ar and H_2 were set to 450 sccm and 50 sccm, respectively. Finally the growth time of graphene was set.

2.2. Preparation of the "quartz glass/graphene film/liquid (water or other liquid)" multilayer film structure

After the growth was complete, all valves were safely closed and the graphene-covered glass was removed. The grown graphene glass was then patterned according to the micro/nano-channel patterns. The specific method of operation was to treat the graphene glass with plasma (18 W, 15 minutes) to remove non-patterned graphene. The treated patterned graphene glass was placed in a clean vessel to further prepare a multilayer film coupled structure. The entire production process is shown in Fig. 1. The first step was the preparation of a polydimethylsiloxane (PDMS) pre-polymer which was thoroughly mixed with a silicone elastomer base and a curing agent in a ratio of 10:1. This mixture was then poured into a template and cured at 60 °C for 2 hours to obtain a microfluidic channel with a size of $6 \times 4 \times 0.05$ mm^3. Next, the patterned graphene-glass and the microfluidic channel were treated with a plasma device (10.5 W, 1 minute), and the microfluidic chip was obtained by permanent bonding (outside the microfluidic channel, an inlet and outlet pipe with a diameter of about 0.5 mm was connected). Finally, the microfluidic chip and prism were bonded by the refractive index matching solution to obtain a multilayer film coupled structure of quartz glass/graphene film/liquid. The graphene was sandwiched at the interface of medium 1 (n_1) and medium 2 (n_2).

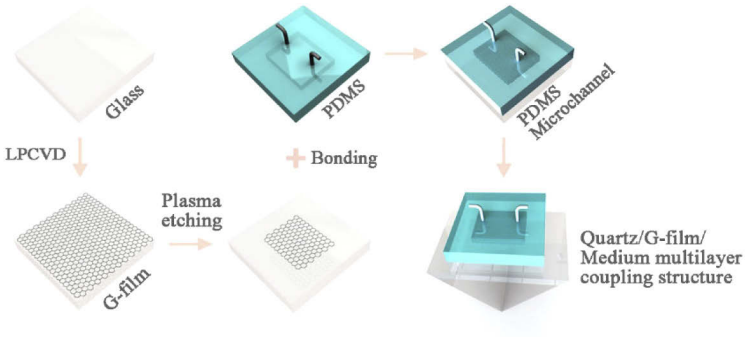

Fig. 1. The entire production process of Quartz glass/Graphene film/Medium multilayer coupling structure.

Optics EXPRESS

2.3. Characterization of graphene

We extensively characterized the graphene-covered glass obtained by LPCVD, and Fig. 2(a) shows an atomic force microscope (AFM, Veeco, Dimension 3100 microscope) image of the obtained graphene film. The left side of the image shows the graphene-covered glass, and the right side is the bare glass substrate, which have a height difference of about 8.13 nm in Fig. 2(b). The AFM image of the left side shows a uniform color in most areas. Figure 2(c) is a high-resolution scanning electron microscope (SEM, America, FEI microscope) image of the graphene film. The SEM image shows that the graphene film has almost no wrinkles because the strong convection of gases in the low-pressure environment ensured the smoothness and flatness of the graphene surface [37]. We also obtained the Raman spectrum of the graphene film (Horiba, LabRAM HR Evolution), as shown in Fig. 2(d), which contains a D peak at 1332.3 cm^{-1}, a G peak at 1562.9 cm^{-1}, and a 2D peak at 2672.9 cm^{-1} [38]. The calculated I_D/I_G was 0.88, which indicates that the graphene has a lower defect level. The samples were also subjected to X-ray photoelectron spectroscopy (XPS) at 1486.6 eV and 400 W. Figure 2(e) shows that the graphene film was mainly composed of carbon (C 1s, 284.85 eV) and oxygen (O 1s, 532.55 eV). The hydrophobicity of the graphene films was analyzed by measuring the static contact angles of the bare glass substrate and the graphene glass using a hydrophilic angle meter (Xuanyichuangxi, XG-CAMB), as shown in the inset of Fig. 2(f). The hydrophobicity of the sensing material has an important influence on the accuracy of microfluidic flow velocity measurement. The better the hydrophobicity of the sensing material is, the smaller the experimental error caused by the viscous resistance between the liquid and the material in the microfluidic chamber is. The static contact angle of the graphene-covered glass (thickness covering of 8 nm to 60 nm) was an average of about 100°, indicating it was hydrophobic, which can reduce the effects of viscous drag generated in microfluidic environments. To further evaluate the macroscopic uniformity and electrical properties of the graphene films, we used a four-probe ohmmeter to monitor the

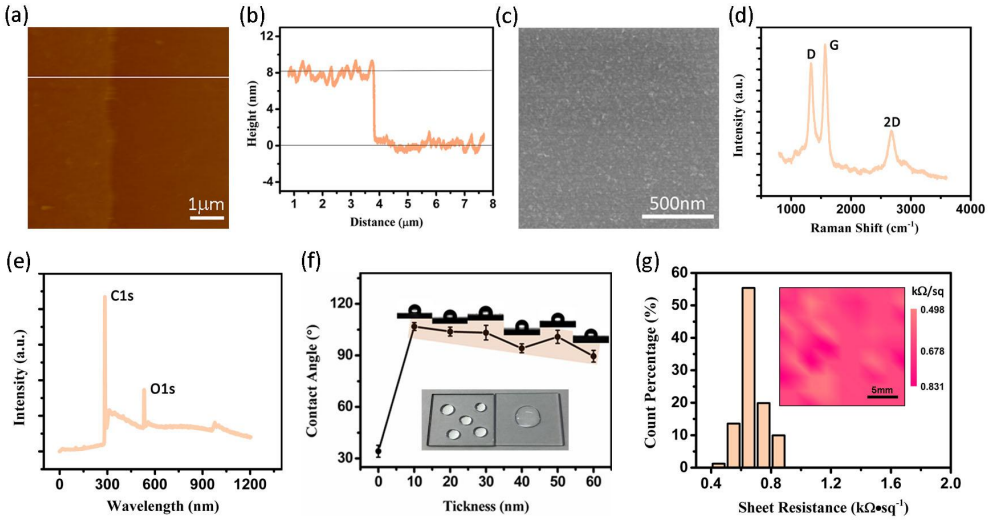

Fig. 2. (a-e) AFM and SEM images, Raman, and XPS spectra of graphene-covered glass grown by ethanol-precursor-based LPCVD. (f) Contact angles measurements of and graphene-covered glass; the inset images show the hydrophobicity of graphene-covered glass and the hydrophilic properties of bare glass. (g) Sheet resistance distribution (collected from 144 points) of the monolayer graphene glass; the inset shows the spatial distribution of the sheet resistance (2 cm × 2 cm).

Optics EXPRESS

sheet resistance of the graphene films (2 cm × 2 cm). The membrane resistance distribution is plotted in Fig. 2(g) (collected from 144 points) and shows a uniform height over most of the surface area. The average sheet resistance was near 0.65 kΩ•sq^{-1}, with maximum and minimum values of 0.85 kΩ•sq^{-1} and 0.45 kΩ•sq^{-1}, respectively, which indicates that the graphene grown by LPCVD has an ultra-uniform sheet resistance and a high electrical conductivity.

3. Experimental and simulation results

3.1. Reflection theory of the "quartz glass/graphene film/liquid (water or other liquid)" multilayer film structure

Graphene has been shown to exhibit different properties for the absorption of the TE mode and TM mode under reflective conditions [29]. The absorption in both the TE and TM modes is sensitive to variations in the refractive index n_2. This effect can be explained by the classic multilayer film reflection theory.

In Fig. 3, graphene ($n_G = 2.73 + 1.35i$) [39] was sandwiched between high-refractive-index medium 1 (quartz glass, $n_1 = 1.47$) and low-refractive-index medium 2 (deionized water, $n_2 = 1.33$). This was called the "quartz glass/graphene film/liquid (water or blood)" multilayer film structure. In the critical total reflection state, a part of the energy can pass through the interface between medium 1 and medium 2, and propagate along the interface to achieve enhanced light-graphene interactions. Regarding the general theory of light refraction and reflection, starting from Maxwell's equations, and using boundary conditions (boundary conditions manifest that the tangential component of an electric field E and magnetic field H are continuous over the boundary), the formula between the incident intensity (A_I), the reflection intensity (A_R), and the transmission intensity (A_T) of the TE mode can be calculated by the following equation:

$$\begin{bmatrix} A_I \\ A_R \end{bmatrix} = \frac{1}{4} \begin{bmatrix} 1 + \frac{k_{gz}}{k_{1z}}\gamma_{1g} & \left(1 - \frac{k_{gz}}{k_{1z}}\gamma_{1g}\right) e^{ik_{gz}d} \\ 1 - \frac{k_{gz}}{k_{1z}}\gamma_{1g} & \left(1 + \frac{k_{gz}}{k_{1z}}\gamma_{1g}\right) e^{ik_{gz}d} \end{bmatrix} \begin{bmatrix} \left(1 + \frac{k_{2z}}{k_{gz}}\gamma_{g2}\right) e^{-ik_{gz}d} \\ 1 - \frac{k_{2z}}{k_{gz}}\gamma_{gz} \end{bmatrix} [A_T] \tag{1}$$

where the subscripts $i = 1, 2, g$ represents medium 1, medium 2, and graphene, respectively. Among them,

$$k_x = n_1 k_0 \sin\theta \ , \ k_{1z} = \sqrt{n_1^2 k_0^2 - k_x^2} \ , \ k_{gz} = \sqrt{n_g^2 k_0^2 - k_x^2} \ , \ k_{2z} = \sqrt{n_2^2 k_0^2 - k_x^2} \ , \ k_0 = \frac{2\pi}{\lambda_0}.$$

where k is the vacuum wave vector, λ_0 is the free space wavelength, θ is the incident angle, γ is the relative permeability, $\gamma_{1g} = \varepsilon_1 / \varepsilon_g$, $\gamma_{g2} = \varepsilon_g / \varepsilon_2$, and μ is the relative magnetic permeability. The relationship between the incident intensity (A_I), the reflection intensity (A_R), and the transmission intensity (A_T) in the TM mode can be obtained by changing the magnetic permeability μ relative to the dielectric constant ε.

3.2. Detection of microfluidic flow velocity with GFS system and simulation of microfluidic flow with Comsol

As shown in Fig. 4, the GFS was configured with a He-Ne linear polarization laser, which passes through an attenuator, a polarizer, and a quarter-wave plate, to obtain stable, power-adjustable, circularly polarized light. The spot formed by the beam is much smaller than the size of the micro-chamber, and the circularly polarized light is separated into TE and TM modes by a Wollaston prism. Both beams have the same optical path, which significantly suppresses common mode noise to obtain relatively stable experimental results [35]. Then, the two beams respectively entered the detection holes of the balance detector, and converted the optical signals into electrical signals.

Optics EXPRESS

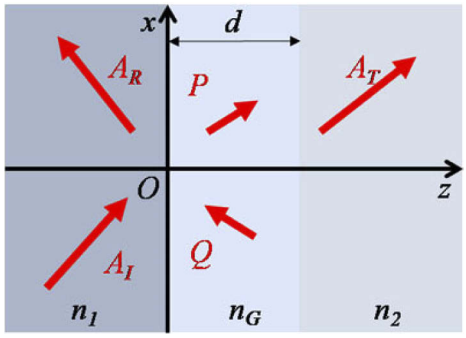

Fig. 3. The theoretical model of the graphene-based optical microfluidic sensor.

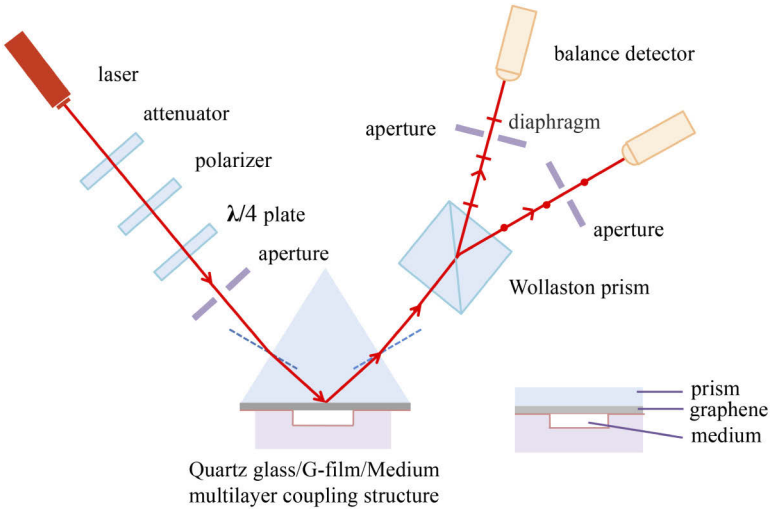

Fig. 4. Experimental setup of the graphene-based microfluidic flow sensing system. The illustration on the right is the cross-sectional image of the multi-layer coupling structure.

This novel GFS responded to fast changes in flow velocity and pressure. In the experiment, the velocity can be estimated according to the liquid flow rate under the condition of continuous liquid flow:

$$v = \frac{dQ}{dS} \tag{2}$$

Where dQ is the volume flow per unit time, and dS is the cross-sectional area of the microfluidic chamber. According to our research, it is found that the relationship between the collected voltage signal and the velocity is approximately linear:

$$\frac{dU}{dv} = 4.65 \times 10^5 mV \cdot sm^{-1} \tag{3}$$

Where dU is the change of voltage signal caused by pressure (also the change of liquid refractive index n_2), dv is the change of liquid velocity signal. To further explore the relationship between pressure and velocity, COMSOL was used to simulate the pressure and flow velocity distribution in the microfluidic chamber. The relationship between the pressure (dP) and velocity

Optics EXPRESS

signal (dv) in microfluidics is established:

$$\frac{dP}{dv} = 9.43 \times 10^5 Pa \cdot sm^{-1} \tag{4}$$

It is proved that there is a linear relationship among pressure, flow velocity and voltage. Here, we made a video to record repeated the application of transient and weak pressure to the system and obtain flow velocity and pressure responses (see Visualization 1). Because of the linear relationship between pressure, flow velocity and voltage, we deem that the trend of voltage signal is similar to the behavioral trend of pressure and flow velocity. Figure 5(a) shows the real-time flow velocity and pressure measurement results due to the transient and weak pressure of the syringe. Here, we extracted a pulse signal and meticulously analyzed the experimental phenomena between 135 and 140 s. Figure 5(b) shows the tendency of the flow velocity and pressure from 135 s to 140 s, which indicated a maximal flow velocity of about 11 mm/s (the corresponding pressure was 1.048×10^4 Pa). The response and recovery times were 0.3 s and 0.6 s, respectively. This behavior was also simulated with imaging, and a trend consistent with the experimental results was obtained. A dynamic image of the theoretical simulation process is provided in Visualization 2, in a 10X slow-motion effect). Figure 5(c) is the extracted simulated flow velocity (or pressure) signal for several specific and representative moments, and visually illustrates the change in fluid velocity (or pressure) within the microfluidic channel. Table 1 shows the voltage, flow velocity, and pressure signals at these specific moments, and shows the linear relationship between the three parameters. This demonstrates that this sensor can be used for the real-time monitoring of complex flow conditions in microfluidic channels and forms an image by scanning in real-time.

Table 1. The voltage, flow velocity, and pressure signals at the specific moments in Fig. 5(c).

	T_1	T_2	T_3	T_4	T_5
Voltage (V)	1.549	1.530	1.683	5.165	3.186
Velocity (mm/s)	3.331	3.290	3.619	11.11	6.852
Pressure (Pa)	3.142×10^3	3.103×10^3	3.414×10^3	1.048×10^4	6.463×10^3
	T_6	T_7	T_8	T_9	
Voltage (V)	2.177	1.816	1.740	1.607	
Velocity (mm/s)	4.682	3.905	3.742	3.456	
Pressure (Pa)	4.416×10^3	3.683×10^3	3.530×10^3	3.260×10^3	

3.3. Simulation by the peristaltic pump of the contraction and expansion of the heart

We used peristaltic pump peristalsis to simulate the contraction and expansion of the heart, and the simulated blood flow signal was detected by the GFS. In general, the difference between the right ventricular systolic and diastolic blood pressure of a normal person is about 2.6 kPa, and the heartbeat frequency is 1 - 1.67 Hz. Here, we performed many simulations to analyze pressure differences and frequency ranges, as shown in Fig. 6(a), Fig. 6(b), and Fig. 7. The simulated experimental results covered the entire range of normal values and were far beyond this range. Their corresponding flow velocity and pressure signals are presented by impulses within the given periods, which are very similar to the electrocardiogram (ECG) signals. The results in Fig. 6(a) are especially similar, with a pressure of 3 kPa and a frequency of 1 Hz, and Fig. 6(b) with a given pressure of 11 kPa and a frequency of 0.1 Hz. When the pump frequency increases, micro-fluctuations appeared in the experimental data. We determined that the disturbance phenomenon in Fig. 6(a) was due to vibrations of the entire simulation environment caused by operating the pump head at a high frequency. Simulated experiments were carried out at low

Optics EXPRESS

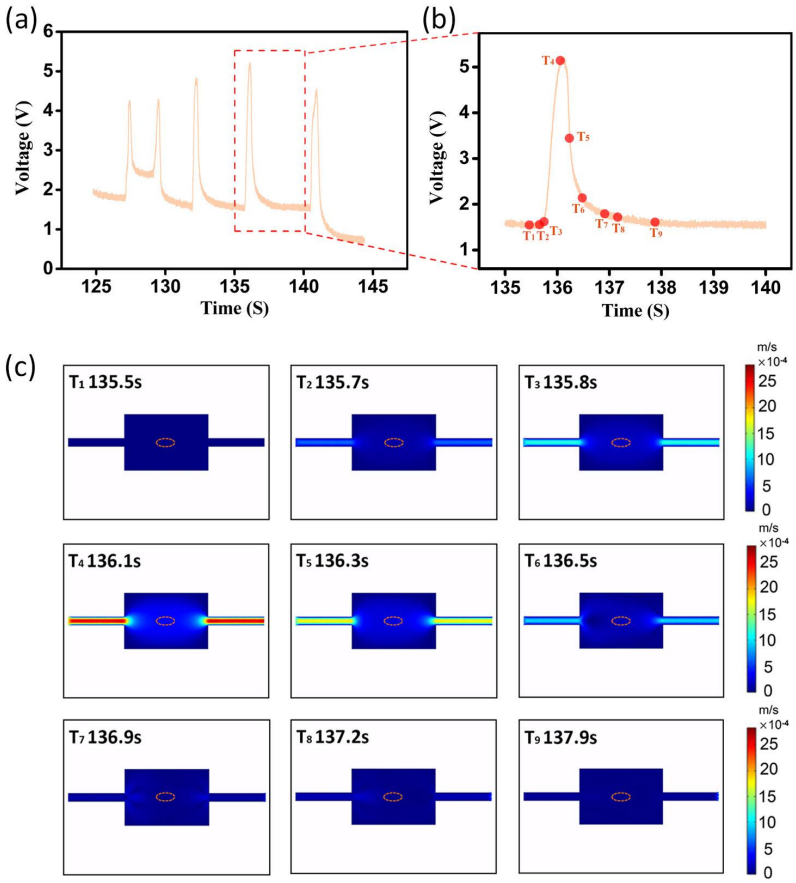

Fig. 5. (a) The voltage-time signal collected from the video. (b) The voltage-time signal between 135 and 140 s. (c) A simulated flow velocity signal for several specific and representative moments.

pump frequencies or at high pump pressures. At a low pump frequency, as shown in Fig. 6(b), the simulated flow velocity (or pressure) stability increased, and there was a noise reduction in the peristaltic pump. This shows that the sensor could accurately detect complex changes in fluid velocities (or pressures). We extracted the period and voltage information from several sets of data, and the statistical results are shown in Fig. 6(c). Each cycle of statistical results is displayed in Fig. 7. Through simulations and statistical analysis, we concluded that: i) the frequency range measured by the GFS system can provide comprehensive coverage of human heartbeats, and a statistically significant voltage response was obtained in the low and high-frequency bands; ii) the system could accurately detect flow velocities and pressures using different pulse pumps. In addition, the voltage (flow velocity or pressure)-time data for low pump frequencies of 0.04 Hz, 0.05 Hz, and 0.06 Hz are shown in Figs. 7(a)–7(c), respectively. When the pumping speed decreased, the period was lengthened, and there was a noise reduction in the peristaltic pump. Due to the high and low-speed settings of the peristaltic pump, different rotation numbers indicate a wide measurement range. The detected signal of the simulated process was far beyond normal levels, which shows that the GFS can detect weak abnormal signals in blood velocity (or pressure) caused by heart or blood vessels. Based on this, we have a prospection that GFS can be applied in the medical field. When some critically ill patients need to use extracorporeal circulation

Optics EXPRESS

machines (such as dialysis therapy), GFS can monitor extracorporeal blood flow velocity; an integrated device can be made to measure blood flow velocity if graphene is coupled to optical fiber. It may indicate vascular blockage, heart failure, and other related diseases.

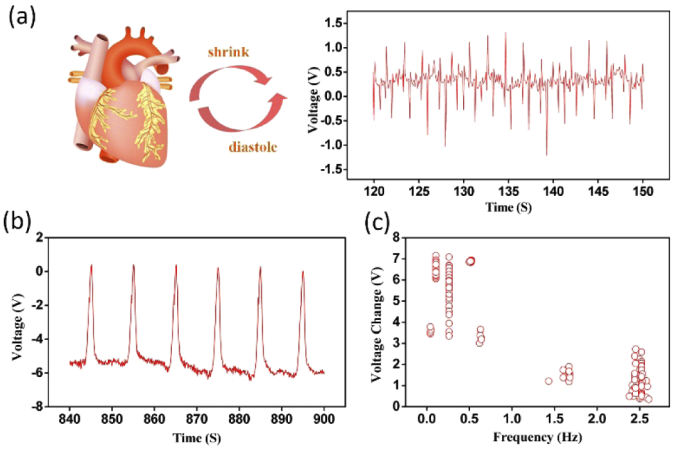

Fig. 6. (a) The voltage-time signal obtained when liquid was pumped at a higher speed. (b) The voltage-time signal obtained when liquid was pumped at a lower speed. (c) The cycle and voltage information in the experimental data was extracted when the peristaltic pump was set to different revolutions.

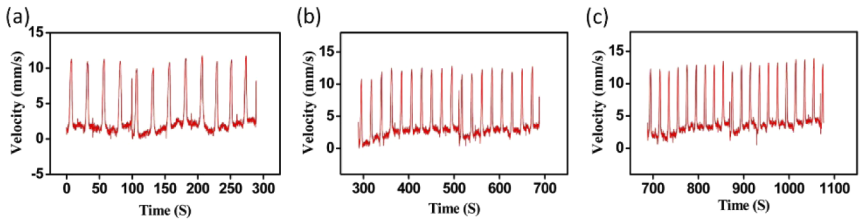

Fig. 7. (a-c) The flow velocity-time data for the peristaltic pump at frequencies of 0.04 Hz, 0.05 Hz, and 0.06 Hz, respectively.

4. Conclusion

By growing high-quality graphene directly on glass substrates, we designed a microfluidic-integrated graphene-based flow sensor (GFS) based on the excellent polarization absorption characteristics of graphene obtained from CVD. This sensor was used to investigate weak and transient flow velocity and pressure signals generated by applying slight pressure to a syringe. The experimental results accurately and clearly showed the pulse flow velocity and pressure signals caused by each uneven pressure application. Based on the theory established by the standard experiments above, we systematically simulated and analyzed single pulse flow velocity (or pressure) signals and established a relationship between the flow velocity and pressure. This sensor was able to monitor simulated blood flow and simulated heart motility. Simulations were performed on the flow velocity, pressure, and pump frequency of the heart and blood vessels. This sensor accurately detected a pumping frequency range from 0.04 Hz to 2.5 Hz, a velocity range from 0.7 mm/s to 15 mm/s, and a pressure range from 0.6 kPa to 14 kPa. These detected parameter ranges covered both normal and abnormal human parameter ranges. These results show that the GFS can accurately detect both normal and abnormal blood velocity and pressure

Optics EXPRESS

signals caused by the heart or blood vessels. These responses may be used to indicate vascular blockage, heart failure, and other related diseases. The GFS may be used for the real-time monitoring of patients' basic vital signs from their blood flow.

Funding

National Natural Science Foundation of China (11604182, 11704227, 61505109); Natural Science Foundation of Shandong Province (ZR2016AB05); Ministry of Education Chunhui Plan Cooperation Research Project (10801X10096030).

Disclosures

The authors declare no conflicts of interest.

References

1. R. K. Jain, "Determinants of tumor blood flow: a review," Cancer Res. **48**(10), 2641–2658 (1988).
2. H. A. Kontos, "Validity of cerebral arterial blood flow calculations from velocity measurements," Stroke **20**(1), 1–3 (1989).
3. D. Attwell, A. M. Buchan, S. Charpak, M. Lauritzen, B. A. MacVicar, and E. A. Newman, "Glial and neuronal control of brain blood flow," Nature **468**(7321), 232–243 (2010).
4. K. K. Mistry and A. Mahapatra, "Design and simulation of a thermo transfer type MEMS based micro flow sensor for arterial blood flow measurement," Microsyst. Technol. **18**(6), 683–692 (2012).
5. N. S. Coverdale, J. S. Gati, O. Opalevych, A. Perrotta, and J. K. Shoemaker, "Cerebral blood flow velocity underestimates cerebral blood flow during modest hypercapnia and hypocapnia," J. Appl. Physiol. **117**(10), 1090–1096 (2014).
6. Y. Ma, G. Li, J. Li, and W. Ren, "The diagnostic value of superb microvascular imaging (SMI) in detecting blood flow signals of breast lesions: a preliminary study comparing SMI to color Doppler flow imaging," Medicine **94**(36), e1502 (2015).
7. L. Zarrinkoob, K. Ambarki, A. Wåhlin, R. Birgander, A. Eklund, and J. Malm, "Blood flow distribution in cerebral arteries," J. Cereb. Blood Flow Metab. **35**(4), 648–654 (2015).
8. K. Kisler, A. R. Nelson, A. Montagne, and B. V. Zlocovic, "Cerebral blood flow regulation and neurovascular dysfunction in Alzheimer disease," Nat. Rev. Neurosci. **18**(7), 419–434 (2017).
9. T. W. Secomb, "Blood flow in the microcirculation," Annu. Rev. Fluid Mech. **49**(1), 443–461 (2017).
10. C. M. Boutry, L. Beker, Y. Kaizawa, C. Vassos, H. Tran, A. C. Hinckley, R. Pfattner, S. Niu, J. Li, J. Claverie, Z. Wang, J. Chang, P. M. Fox, and Z. Bao, "Biodegradable and flexible arterial-pulse sensor for the wireless monitoring of blood flow," Nat. Biomed. Eng. **3**(1), 47–57 (2019).
11. T. Tanaka and G. B. Benedek, "Measurement of the velocity of blood flow (in vivo) using a fiber optic catheter and optical mixing spectroscopy," Appl. Opt. **14**(1), 189–196 (1975).
12. M. Midttun, P. Sejrsen, and M. C. Jørgensen, "Heat-washout: a new method for measuring cutaneous blood flow rate in areas with and without arteriovenous anastomoses," Clin. Physiol. **16**(3), 259–274 (1996).
13. G. A. Holloway Jr. and D. W. Watkins, "Laser Doppler measurement of cutaneous blood flow," J. Invest. Dermatol. **69**(3), 306–309 (1977).
14. K. Kijsamanmith, N. Vongsavan, and B. Matthews, "Pulpal blood flow recorded from exposed dentine with a laser Doppler flow meter using red or infrared light," Arch. Oral Biol. **87**, 163–167 (2018).
15. M. Sorelli, P. Francia, L. Bocchi, A. De Bellis, and R. Anichini, "Assessment of cutaneous microcirculation by laser Doppler flowmetry in type 1 diabetes," Microvasc. Res. **124**, 91–96 (2019).
16. K. S. Kim, Y. Zhao, H. Jang, S. Y. Lee, J. M. Kim, K. S. Kim, J. H. Ahn, P. Kim, J. Y. Choi, and B. H. Hong, "Large-scale pattern growth of graphene films for stretchable transparent electrodes," Nature **457**(7230), 706–710 (2009).
17. F. Bonaccorso, Z. Sun, T. Hasan, and A. C. Ferrari, "Graphene photonics and optoelectronics," Nat. Photonics **4**(9), 611–622 (2010).
18. M. Engel, M. Steiner, A. Lombardo, A. C. Ferrari, H. V. Löhneysen, P. Avouris, and R. Krupke, "Light–matter interaction in a microcavity-controlled graphene transistor," Nat. Commun. **3**(1), 906 (2012).
19. O. V. Kotov, M. A. Kol'chenko, and Y. E. Lozovik, "Ultrahigh refractive index sensitivity of TE-polarized electromagnetic waves in graphene at the interface between two dielectric media," Opt. Express **21**(11), 13533–13546 (2013).
20. Y. Wu, B. Yao, A. Zhang, Y. Rao, Z. Wang, Y. Cheng, Y. Gong, W. Zhang, Y. Chen, and K. S. Chiang, "Graphene-coated microfiber Bragg grating for high-sensitivity gas sensing," Opt. Express **39**(5), 1235–1237 (2014).
21. Y. Xiao, J. Yu, L. Shun, S. Tan, X. Cai, Y. Luo, J. Zhang, H. Dong, H. Lu, H. Guan, Y. Zhong, J. Tang, and Z. Chen, "Reduced graphene oxide for fiber-optic toluene gas sensing," Opt. Express **24**(25), 28290–28302 (2016).

Optics EXPRESS

22. J. F. Wu, H. T. Wang, Z. W. Su, M. H. Zhang, X. D. Hu, Y. J. Wang, Z. A. Wang, B. Zhong, W. W. Zhou, J. P. Liu, and S. G. Xing, "Highly flexible and sensitive wearable E-skin in mass industry production available," ACS Appl. Nano Mater. **9**(44), 38745–38754 (2017).
23. K. P. W. Dissanayake, W. Wu, H. Nguyen, T. Sun, and K. T. V. Grattan, "Graphene-Oxide-Coated Long-Period Grating-Based Fiber Optic Sensor for Relative Humidity and External Refractive Index," Opt. Express **36**(4), 1145–1151 (2018).
24. J. F. Wu, Z. Y. Ma, Z. Hao, J. T. Zhang, P. F. Sun, M. H. Zhang, Y. K. Liu, Y. S. Cheng, Y. Li, B. Zhong, T. Zhang, L. Xia, W. Yao, X. X. Huang, H. T. Wang, H. P. Liu, F. Yan, E. C. Hsu, and G. Z. Xing, "Sheath–Core Fiber Strain Sensors Driven by in-Situ Crack and Elastic Effects in Graphite Nanoplate Composites," ACS Appl. Nano Mater. **2**(2), 750–759 (2019).
25. Z. W. Li, W. F. Zhang, and F. Xing, "Graphene Optical Biosensors," Int. J. Mol. Sci. **20**(10), 2461 (2019).
26. F. Xing, Z. B. Liu, Z. C. Deng, X. T. Kong, X. Q. Yan, X. D. Chen, Q. Ye, C. P. Zhang, Y. S. Chen, and J. G. Tian, "Sensitive real-time monitoring of refractive indexes using a novel graphene-based optical sensor," Sci. Rep. **2**(1), 908 (2012).
27. F. Xing, G. X. Meng, Q. Zhang, L. T. Pan, P. Wang, Z. B. Liu, W. S. Jiang, Y. S. Chen, and J. G. Tian, "Ultrasensitive flow sensing of a single cell using graphene-based optical sensors," Nano Lett. **14**(6), 3563–3569 (2014).
28. F. Xing, Y. Yang, J. F. Shen, W. S. Jiang, Z. B. Liu, S. W. Zhu, and X. C. Yuan, "Ultra-high sensitivity, multi-parameter monitoring of dynamical gas parameters using a reduced graphene oxide microcavity," Sens. Actuators, B **235**, 474–480 (2016).
29. Q. Ye, J. Wang, Z. B. Liu, Z. C. Deng, X. T. Kong, F. Xing, X. D. Chen, W. Y. Zhou, C. P. Zhang, and J. G. Tian, "Polarization-dependent optical absorption of graphene under total internal reflection," Appl. Phys. Lett. **102**(2), 021912 (2013).
30. X. S. Li, W. W. Cai, J. H. An, S. Kim, J. H. Nah, D. X. Yang, R. Piner, A. Velamakanni, I. H. Jung, E. Tutuc, S. K. Banerjee, L. Colombo, and R. S. Ruoff, "Large-area synthesis of high-quality and uniform graphene films on copper foils," Science **324**(5932), 1312–1314 (2009).
31. M. Taghioskoui, "Trends in graphene research," Mater. Today **12**(10), 34–37 (2009).
32. P. H. Wang, Z. Q. Li, W. J. Salcedo, Z. Sun, S. M. Huang, and A. G. Brolo, "Surface plasmon enhanced up-conversion from $NaYF_4$: Yb/Er/Gd nano-rods," Phys. Chem. Chem. Phys. **17**(24), 16170–16177 (2015).
33. S. Bhaviripudi, X. T. Jia, M. S. Dresselhaus, and J. Kong, "Role of kinetic factors in chemical vapor deposition synthesis of uniform large area graphene using copper catalyst," Nano Lett. **10**(10), 4128–4133 (2010).
34. X. D. Chen, Z. L. Chen, W. S. Jiang, C. Zhang, J. Y. Sun, H. H. Wang, W. Xin, L. Li, M. K. Priydarshi, H. Yang, Z. B. Liu, J. G. Tian, Y. Y. Zhang, Y. F. Zhang, and Z. F. Liu, "Fast growth and broad applications of 25-inch uniform graphene glass," Adv. Mater. **29**(1), 1603428 (2017).
35. B. Hou, R. Xiang, T. Inoue, E. Einarsson, S. Chiashi, J. Shiomi, A. Miyoshi, and S. Maruyama, "Decomposition of ethanol and dimethyl ether during chemical vapor deposition synthesis of single-walled carbon nanotubes," Jpn. J. Appl. Phys. **50**(6R), 065101 (2011).
36. R. Xiang, B. Hou, E. Einarsson, P. Zhao, S. Harish, K. Morimoto, Y. Miyauchi, S. Chiashi, Z. K. Tang, and S. Maruyama, "Carbon atoms in ethanol do not contribute equally to formation of single-walled carbon nanotubes," ACS Nano **7**(4), 3095–3103 (2013).
37. H. Lu, L. Y. Koo, W. M. Wang, D. A. Lauffenburger, L. G. Griffith, and K. F. Jensen, "Microfluidic shear devices for quantitative analysis of cell adhesion," Anal. Chem. **76**(18), 5257–5264 (2004).
38. A. C. Ferrari, J. C. Meyer, V. Scardaci, C. Casiraghi, M. Lazzeri, F. Mauri, S. Piscanec, D. Jiang, K. S. Novoselov, S. Roth, and A. K. Geim, "Raman spectrum of graphene and graphene layers," Phys. Rev. Lett. **97**(18), 187401 (2006).
39. J. W. Weber, V. E. Calado, and M. C. M. Van De Sanden, "Optical constants of graphene measured by spectroscopic ellipsometry," Appl. Phys. Lett. **97**(9), 091904 (2010).